Theory and Realization of Nonresonant Anisotropic Singly Polarized Solids Carrying Only Shear Waves

Mingye Zheng,[1,‡] Xiaoning Liu,[1,‡] Yi Chen,[1] Hongchen Miao,[2] Rui Zhu,[1,*] and Gengkai Hu[1,†]

[1] *Key Laboratory of Dynamics and Control of Flight Vehicle, Ministry of Education, School of Aerospace Engineering, Beijing Institute of Technology, Beijing 100081, China*

[2] *Applied Mechanics and Structure Safety Key Laboratory of Sichuan Province, School of Mechanics and Engineering, Southwest Jiaotong University, Chengdu, Sichuan 610031, China*

(Received 31 March 2019; revised manuscript received 10 June 2019; published 15 July 2019)

Due to the complex polarizations of waves in elastic media, achieving broadband wave engineering in elastic metamaterials (EMMs) proves to be much more difficult than in the acoustic or electromagnetic counterparts. By designing a nonresonance-based singly polarized solid (SPS) with deep-subwavelength scale microstructures, we experimentally demonstrate that elastic wave polarization can be tailored in a broad frequency range. With an inverse design on the EMM's elasticity tensor, interesting wave behavior in a "fluidlike solid" or "shear-wave solid" can be achieved. By measuring the longitudinal as well as shear wave's propagation through the fabricated SPS layers with less than 1/20λ thickness, nearly total transmission or reflection for the targeted wave polarizations can be observed at different frequencies. Our work opens an alternative avenue for broadband elastic metamaterials design based on wave polarization engineering with various potential applications in the fields of structural monitoring, elastic wave communications, and ultrasonic elastography.

DOI: 10.1103/PhysRevApplied.12.014027

I. INTRODUCTION

Collective particles vibrating at their equilibrium positions transmit energy to the targeted place in the form of a wave. The particle vibrating direction, known as polarization, is dependent on the material's properties with two extremes: parallel and perpendicular to the wave propagating direction, defined as longitudinal (L) and transverse (T) waves, respectively. In nature, inviscid fluids support only L waves while solids carry both types of waves simultaneously. It is of interest to ask whether a material transmitting only shear waves (T waves in solids) exists and whether a solid carrying only L waves as a liquid could be designed. Beyond any doubt, innovations in wave engineering could be imagined if these kinds of metamaterials are at hand, such as nondestructive evaluation, elastic wave communication, and ultrasonic elastography [1–5].

Metamaterials with well-designed locally resonant (LR) microstructures provide an unprecedented manner to manipulate waves at a deep subwavelength scale [6–9]. While electromagnetic and acoustic metamaterials are designed for transverse electromagnetic waves [10–12] and longitudinal pressure waves [13–15], respectively, elastic metamaterials (EMMs) attract growing attention for their ability to manipulate both L and T waves [16–25]. For example, with the introduction of a subwavelength-scale monopolar, dipolar, or quadrupolar resonator, the effective bulk modulus, mass density, or shear modulus of the EMM can be negative, respectively, and therefore, prohibits the corresponding type of elastic wave propagation in a specific band gap near the resonant frequencies [26]. Peculiar wave trajectory controls, such as negative refraction or cloaking, could be realized by the LR-induced double negativity or/and anisotropic mass density [27–29]. By opening a Dirac cone and forming a band gap, topologically protected edge wave transmission can be realized with its backscattering immunity and robust energy transport [30–32]. It should be pointed out that the above wave manipulations can only be achieved in or near a band gap, which, although it can be widened with specific metamaterial designs [33,34], is still within a limited frequency range. More recently, elastic wave mode conversion has attracted growing attention due to its uniqueness compared with acoustic waves and potential applications in various engineering fields. Transmodal Fabry-Pérot resonance can be utilized to achieve almost total mode conversion at periodic frequency points instead of a continuous frequency range [35–37].

In order to achieve broadband elastic wave control without the limitations from the resonance-based band gap,

*rzhu83ac@gmail.com
†hugeng@bit.edu.cn
‡Both authors contributed equally to this work

 © 2019 American Physical Society

nonresonant EMMs should be investigated and the relationship between the wave polarization and the stiffness tensors of the EMMs needs to be studied systematically in a quasistatic framework. Milton and Cherkaev [38] distinguish the deformation modes from a material by classifying them with the number of vanishing eigenvalues in the stiffness tensor. To our knowledge, engineering polarization through subtle material microstructure design is rare, although this situation slows down the device and material designs for manipulating specific elastic polarization.

In this paper, the relationships between the wave polarization and stiffness tensors of different solids are first systematically investigated. Then the concept of "singly polarized solids (SPSs)" is proposed by designing a type of nonresonant EMM. In particular, subwavelength-scale anisotropic SPSs are engineered to permit only L wave or T wave propagation in a very wide continuous frequency range as long as the long wavelength condition is satisfied. What is more, L-wave-only and T-wave-only supportability can mutually transfer from one to the other by just rotating the principal orientation of the SPS. The corresponding microstructure design of the EMM is realized by using the numerically based effective medium method. The broad-band "wave polarization control" abilities of the EMM are experimentally demonstrated. Finally, potential applications of the EMM are also explored for alternative elastic wave devices, such as a 90° polarized wave splitter and polarized wave focusing.

II. THEORY OF ELASTIC WAVE POLARIZATION ENGINEERING

First, let us consider elastic wave propagation in a solid with general anisotropy. The governing equation can be written as

$$C_{ijkl}u_{k,l_i} = \rho \ddot{u}_j, \tag{1}$$

where ρ is the mass density and C_{ijkl} is the fourth-order stiffness tensor. For harmonic wave propagations, the displacement $u_l = U_l e^{i(-k_j x_j + \omega t)}$ (i denotes the imaginary unit) is assumed. Without loss of generality, we consider a two-dimensional (2D) problem in this research. By substituting the harmonic displacement into Eq. (1), an eigenvalue problem can be obtained with the following components of k_j, u_j, and C_{rs} ($i, j, k, l = 1$ and 2; $r, s = 1$, 2, and 6) as

$$\begin{bmatrix} A_{11}^* & A_{12}^* \\ A_{21}^* & A_{22}^* \end{bmatrix} \begin{bmatrix} U_1 \\ U_2 \end{bmatrix} = 0, \tag{2a}$$

where

$$\begin{cases} A_{11}^* = k_1^2 C_{11} + 2k_1k_2C_{16} + k_2^2 C_{66} - \rho\omega^2. \\ A_{12}^* = A_{21}^* = k_1k_2C_{12} + k_1^2 C_{16} + k_2^2 C_{26} + k_1k_2C_{66}. \\ A_{22}^* = k_2^2 C_{22} + 2k_1k_2C_{26} + k_1^2 C_{66} - \rho\omega^2. \end{cases} \tag{2b}$$

It should be noted that the index contraction of the fourth-order tensor C_{ijkl} is applied (see details in Appendix A). By defining a tangent angle, $\tan\varphi = k_2/k_1$, which is related to the wave direction, and considering the nontrivial solution ($A_{11}^* A_{22}^* - A_{12}^* A_{21}^* = 0$) for Eq. (2a), one can obtain the angle ψ related to the particles' vibrations as

$$\begin{aligned} \psi_{1,2} &= \tan^{-1}(U_2/U_1) \\ &= \tan^{-1}\left[\frac{-A + B \pm \sqrt{(A-B)^2 + 4A_{12}^2}}{2A_{12}}\right], \end{aligned} \tag{3a}$$

where

$$\begin{cases} A = C_{11} + 2C_{16}\tan\varphi + C_{66}\tan^2\varphi. \\ B = C_{22}\tan^2\varphi + 2C_{26}\tan\varphi + C_{66}. \\ A_{12} = C_{12}\tan\varphi + C_{16} + C_{26}\tan^2\varphi + C_{66}\tan\varphi. \end{cases} \tag{3b}$$

In order to investigate the elastic wave polarization characteristics in solids, the squares of wave velocity, $c^2 = \omega^2/k^2$, and the corresponding angles of wave polarization, $\theta = \psi - \varphi$, which are defined as the angles between the vibration direction and wave direction, which can then be calculated as

$$c_{1,2}^2 = \frac{(A+B) \pm \sqrt{(A-B)^2 + 4A_{12}^2}}{2\rho(1+\tan^2\varphi)}, \tag{4a}$$

and

$$\theta_{1,2} = \tan^{-1}\left[\frac{-A + B \pm \sqrt{(A-B)^2 + 4A_{12}^2} - 2A_{12}\tan\varphi}{2A_{12} + (-A + B \pm \sqrt{(A-B)^2 + 4A_{12}^2})\tan\varphi}\right], \tag{4b}$$

respectively. This indicates that there are always two polarized elastic waves with the above phase velocities and polarization angles coexisting in common solids in 2D cases. It should be noted that the obtained polarized wave results can also easily be adapted in three-dimensional (3D) cases. Meanwhile, with the quantitative relationship between the wave polarization and the stiffness tensor obtained in Eq. (4), inverse designs for engineered solids having targeted wave polarization characteristics are possible.

A. Conventional solids supporting two polarized elastic waves

It is well known that conventional solids support two propagating elastic body waves with different polarizations in a 2D case. By observing Eq. (4b), it is noted that the two polarization angles, $\theta_{1,2}$, change with the wave direction in solids with anisotropic stiffness tensor. It is also interesting to find that $\tan\theta_1 \times \tan\theta_2 \equiv -1$, which means that the

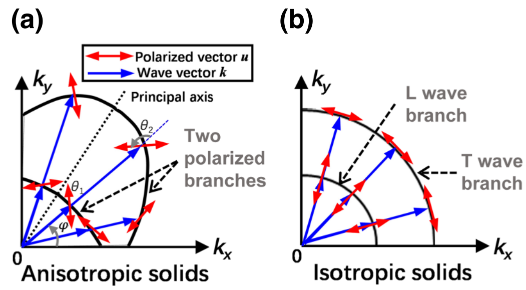

FIG. 1. Supportability of polarized elastic waves in conventional solids. (a), (b) EFCs with polarization information of anisotropic solids (Graphite epoxy resin composite.) (a), isotropic solids (b).

two wave polarization directions are always perpendicular to each other. Figure 1(a) shows the equifrequency curve (EFC) of an anisotropic solid (graphite epoxy resin composite) with its wave polarization information obtained when Eq. 4(b) is added. Obviously, the two EFCs mean that two polarized elastic wave branches coexist in the solid. Although the polarization angles, $\theta_{1,2}$, vary with the wave direction angle, φ, $|\theta_1 - \theta_2| \equiv \pi/2$ can be found for any given φ as predicted above.

Finding a solid that supports both L and T waves omnidirectionally can be a simple inverse problem with one of the following two sets of conditions needing to be satisfied

$$\begin{cases} c_1^2 \neq c_2^2 > 0 \\ \theta_1 \equiv 0 \\ \theta_2 \equiv \pi/2 \end{cases} \quad \text{or} \quad \begin{cases} c_1^2 \neq c_2^2 > 0 \\ \theta_1 \equiv \pi/2 \\ \theta_2 \equiv 0 \end{cases}. \tag{5}$$

By substituting Eqs. (3b) and (4) into Eq. (5), the solid supporting omnidirectional L and T wave propagations can be found with the stiffness tensor having $C_{11} = C_{22} = C_{12} + 2C_{66}$, and $C_{16} = C_{26} = 0$, indicating, as expected, an isotropic solid, as shown in Fig. 1(b).

B. Engineered solids supporting singly polarized elastic wave

Finding an engineered solid that supports only one polarized wave is a very interesting yet difficult inverse problem. In solid mechanics, the elastic property of a material can be characterized by a fourth-order elasticity tensor. Since a general fourth-order elasticity tensor can be expressed by a 6×6 symmetric matrix that has six eigenvalues accompanied with corresponding deformation modes, an "easy deformation mode" can be defined as the one where the corresponding eigenvalue is zero [38]. Here, the word "easy" means that even without external loading, the material can deform proportionally to a special strain state infinitely as water flows. What is more, vanishing or very small eigenvalues of the stiffness tensor can be realized through delicately designed microstructures, which could lead to the degenerated solids mentioned above with different numbers of easy deformation modes [38–40]. Such relaxations in the static deformation could further change the dynamic behavior of the engineered solids. For example, a degenerated isotropic solid with five easy deformation modes, a so-called pentamode material, has been reported to support only L wave propagation [41–44]. Dynamically, this solid behaves like a fluid, which can be very useful in designing underwater cloaks and sonar lenses [45,46]. Unfortunately, the back side of the coin, a solid that supports only T (or shear) wave propagation ($c_L = 0$ or $c_T \gg c_L$), has not been found yet. If the velocities of L and T waves are used as the vertical and horizontal axes, respectively, to create a 2D chart, as shown in Fig. 2(a), no natural or engineered solid can be found on or near the horizontal axis of the chart. To

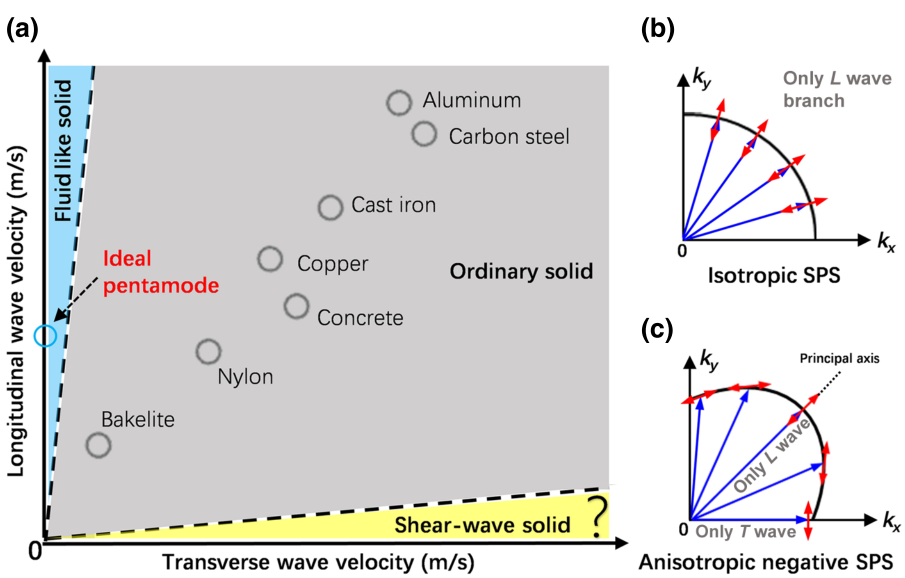

FIG. 2. Supportability of polarized elastic waves in SPS. (a) Schematic diagram of the longitudinal and transverse waves' supportability in common solids. (b), (c) EFCs with polarization information of isotropic SPS ($\gamma = 1$) (b) and anisotropic negative SPS ($\gamma = -1$) (c).

find such a kind of special solids, the wave characteristics of a degenerated solid or SPS should be studied systematically under the framework of the polarization theory we proposed previously.

Two cases are considered for the inverse problem of finding the required stiffness tensor components for a SPS. In Case 1, $c_1^2 > 0$ and $c_2^2 < 0$ are required, which guarantees that only one polarized wave with c_1 is supported in the solid. Thus, the corresponding condition $AB - A_{12}^2 < 0$ can be obtained from Eq. (4a). However, by substituting Eq. (3b) into $AB - A_{12}^2 < 0$, it is found that the corresponding stiffness tensor has a negative definiteness, which violates the thermodynamics law [38], and therefore, should be ignored.

In Case 2, $c_1^2 > 0$ and $c_2^2 = 0$ are required, which also results in singly polarized wave propagation. Similarly, one can obtain the following equation

$$\begin{cases} AB - A_{12}^2 = 0. \\ A + B > 0. \end{cases} \tag{6}$$

By substituting Eq. (3b) into Eq. (6), one can have

$$\begin{cases} C_{11}C_{66} - C_{16}^2 = 0, \\ C_{22}C_{66} - C_{26}^2 = 0, \\ C_{11}C_{22} - C_{12}^2 = 0, \end{cases} \tag{7}$$

with the elasticity matrix under the principal directions being

$$C = \begin{bmatrix} C_{11}^S & \gamma\sqrt{C_{11}^S C_{22}^S} & 0 \\ \gamma\sqrt{C_{11}^S C_{22}^S} & C_{22}^S & 0 \\ 0 & 0 & 0 \end{bmatrix}, \tag{8}$$

where $\gamma = \pm 1$ is introduced due to the square root operation and stands for the positive or negative Poisson ratio of SPS, respectively. C_{11}^S and C_{22}^S are the moduli of SPS along the two principal directions. Furthermore, by substituting Eq. (8) into the expressions of c_1 and θ_1 in Eq. (4), the wave velocity c^S as well as polarization angle θ^S in a SPS are obtained as

$$(c^S)^2 = \frac{C_{11}^S + C_{22}^S \tan^2\varphi}{\rho^S(1 + \tan^2\varphi)}, \tag{9a}$$

and

$$\theta^S = \tan^{-1}\left[\frac{\left(\sqrt{C_{22}^S} - \gamma\sqrt{C_{11}^S}\right)\tan\varphi}{\gamma\sqrt{C_{11}^S} + \sqrt{C_{22}^S}\tan^2\varphi}\right], \tag{9b}$$

respectively.

It is obvious that by requiring $C_{11}^S = C_{22}^S$ and $\gamma = 1$ in Eq. (9b), one can get $\theta^S \equiv 0$ for an arbitrary value of φ, which indicates that this SPS functions exactly the same as the inviscid fluids (water, air, etc.) that support L-wave-only propagation omnidirectionally, as shown in Fig. 2(b). However, to answer the question of whether there exists a SPS that permits only T wave omnidirectionality is more difficult. By requiring $\theta^S \equiv \pi/2$ in Eq. (9b), the equation is valid only when $\gamma = -1$ and $\varphi = \tan^{-1}\sqrt[4]{C_{11}^S/C_{22}^S}$ are satisfied. The interpretations to the solution are: (1) SPS supporting T wave omnidirectionality does not exist. (2) Only SPS with the negative Poisson ratio ($\gamma = -1$) can support a T-wave-only state along its off-principal directions at $\varphi = \tan^{-1}\sqrt[4]{C_{11}^S/C_{22}^S}$, as shown in Fig. 2(c). The elasticity matrix of the corresponding negative SPS under the principal directions is then obtained as follows:

$$C = \begin{bmatrix} C_{11}^S & -\sqrt{C_{11}^S C_{22}^S} & 0 \\ -\sqrt{C_{11}^S C_{22}^S} & C_{22}^S & 0 \\ 0 & 0 & 0 \end{bmatrix}. \tag{10}$$

It should be also noted that when $\varphi = 0$ or $\pi/2$, θ^S equals zero, the negative SPS ($\gamma = -1$) can support the L-wave-only propagation along its principal directions. This interesting phenomenon will be validated numerically and experimentally in the following sections.

III. MICROSTRUCTURE DESIGN

Based on the understandings of the polarized wave supportability in solids, the microstructure designs and optimizations of targeted SPSs such as Eq. (10) are conducted in this section, which also serve as the basis for subsequent experiments and simulations.

A. Numerically based effective medium method for SPS design

Considering the detailed geometry of the microstructure, the effective properties of a SPS are extracted by using the numerically based effective medium method [47]. First, since no resonance phenomenon is expected under the long wavelength condition, the effective density ρ^{eff} can be simply calculated from the volume average as $\rho^{\text{eff}} = \rho_s V_s / V_{\text{cell}}$, where ρ_s and V_s denote the density and volume of the base material, respectively, while V_{cell} denotes the volume of the unit cell. Second, the effective stiffness of the SPS can be retrieved from its dispersion curve. Because of the zero definiteness of the stiffness matrix in Eq. (8), a perfect SPS design can only exist as an ideal case. For practically designed SPSs, the effective stiffness matrix should take the following form with a tiny shear modulus C_{66}^{eff} in its principal coordinates in order to satisfy the stability requirement

$$C = \begin{bmatrix} C_{11}^{\text{eff}} & C_{12}^{\text{eff}} & 0 \\ C_{12}^{\text{eff}} & C_{22}^{\text{eff}} & 0 \\ 0 & 0 & C_{66}^{\text{eff}} \end{bmatrix}. \tag{11}$$

Thus, the phase velocity of the medium in different directions can be obtained by substituting Eqs. (11) and (3b) into Eq. (4a) as follows:

$$\begin{cases} c_{L1}^2 = C_{11}^{\text{eff}}/\rho^{\text{eff}}, c_{T1}^2 = C_{66}^{\text{eff}}/\rho^{\text{eff}}, \\ c_{L2}^2 = C_{22}^{\text{eff}}/\rho^{\text{eff}}, \\ c_{qL}^2 = \left[C_{11}^{\text{eff}} + C_{22}^{\text{eff}} + 2C_{66}^{\text{eff}} + \sqrt{(C_{11}^{\text{eff}} - C_{22}^{\text{eff}})^2 + 4(C_{12}^{\text{eff}} + C_{66}^{\text{eff}})^2}\right] \Big/ (4\rho^{\text{eff}}), \\ c_{qT}^2 = \left[C_{11}^{\text{eff}} + C_{22}^{\text{eff}} + 2C_{66}^{\text{eff}} - \sqrt{(C_{11}^{\text{eff}} - C_{22}^{\text{eff}})^2 + 4(C_{12}^{\text{eff}} + C_{66}^{\text{eff}})^2}\right] \Big/ (4\rho^{\text{eff}}), \end{cases} \tag{12}$$

where c_{L1}, c_{T1}, c_{L2} denote the phase velocity of the L wave along the 1-direction, the phase velocity of the T wave along the 1-direction, and the phase velocity of the L wave along the 2-direction, respectively (1 and 2 are the principal orientations of the SPS). c_{qL} and c_{qT} denote the phase velocities of the L and T waves along a 45° angle to the 1-direction, respectively. The above phase velocities can be obtained numerically by calculating the slopes of the dispersion curves near the origin point. Finally, the effective stiffness can be obtained as follows:

$$\begin{cases} C_{11}^{\text{eff}} = \rho^{\text{eff}} c_{L1}^2, C_{22}^{\text{eff}} = \rho^{\text{eff}} c_{L2}^2, C_{66}^{\text{eff}} = \rho^{\text{eff}} c_{T1}^2, \\ C_{12}^{\text{eff}} = \rho^{\text{eff}}[\pm\sqrt{(c_{qL}^2 - c_{qT}^2)^2 - (c_{L1}^2 - c_{L2}^2)^2/4} - c_{T1}^2], \end{cases} \tag{13}$$

where the choice of "+" or "−" depends on the positive or negative sign of γ.

B. Microstructure design and optimization

From Eq. (10), it can be found that only the L wave can propagate along the principal directions of the SPS while the T wave is completely blocked when $\varphi = 0$ (or $\pi/2$). However, the situation is totally different when $\varphi = \tan^{-1}\sqrt[4]{C_{11}^S/C_{22}^S}$, meaning that only the T wave propagates while the L wave is completely blocked. Therefore, in order to verify the above totally different wave performances of the SPS, one-dimensional (1D) wave filtering of the targeted polarized elastic waves is performed. Here, we assume the wave vector is always along the x direction, so the angle φ can be manipulated by rotating the principal orientation of the SPS. Specifically, two cases are considered. For Case 1, the L wave can totally pass through the SPS with $\varphi = 0$, while the T wave is completely blocked as shown in Fig. 3(a). For Case 2, the T wave can totally pass through the SPS with $\varphi = \tan^{-1}\sqrt[4]{C_{11}^S/C_{22}^S}$, while the L wave is completely blocked as shown in Fig. 3(b). Obviously, the complete blocking of the T wave (or L wave) in Case 1 (or 2) is able to be realized by the SPS whose elasticity matrix satisfies Eq. (10). Also, the complete transmission of the L wave (or T wave) in Case 1 (or 2) is closely related to the degree of corresponding impedance matching between the SPS and the background

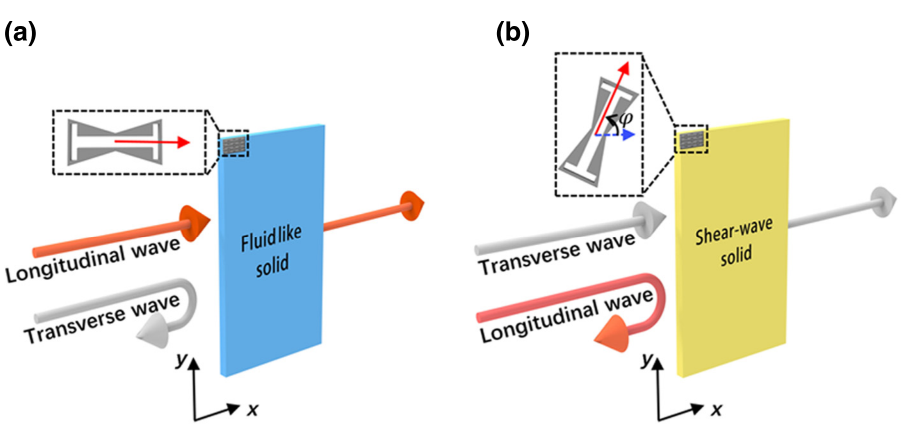

FIG. 3. The desired polarized elastic wave filtering properties based on the proposed SPS. (a), (b) Total transmission and reflection achieved in the desired SPS for the L and T wave propagations along (a) or off (b) the principal axis.

medium. Therefore, we need to further restrict C_{11}^S, C_{22}^S in Eq. (10). Here, we assume that the elasticity matrix of the background medium under the same reference coordinate system is as follows:

$$C = \begin{bmatrix} C_{11}^0 & C_{12}^0 & 0 \\ C_{12}^0 & C_{22}^0 & 0 \\ 0 & 0 & C_{66}^0 \end{bmatrix}. \tag{14}$$

In order to perfectly match the impedance between the SPS and background medium, we find that C_{11}^S, C_{22}^S need to satisfy the following relationship (see details in Appendix B).

$$\begin{cases} C_{11}^S = (\rho^0/\rho^S)C_{11}^0, \\ C_{22}^S = (\rho^0/\rho^S)(C_{66}^0)^2/C_{11}^0, \end{cases} \tag{15}$$

where ρ^S, ρ^0 denote the densities of SPS and the background medium, respectively. Thus Eq. (15) can be regarded as the optimization objective in our following work.

First, a simplified microstructure design of the SPS is developed based on the previous work of an anisotropic pentamode material done by Chen *et al.* [47]. As shown in a single unit cell in Fig. 4(a), the overall shear rigidity can be adjusted by changing the width of the lattice frame, which has the lattice constants a and b along the x and y directions, respectively. The angle between the tilting side of the unit cell and the y axis is β. Inside the hexagonal unit cell, two slots with length l_y, width w_y and one slot with length l_x, width w_x are cut along the vertical and horizontal directions, respectively. Four trapezoid solid parts inside the dashed regions function as "attached masses" for the wave impedance adjustment. We can extract the effective material parameters from the SPS microstructure by using the numerically based effective medium method proposed previously.

Then, we can optimize the geometric parameters $(\beta, a, b, l_x, w_x, l_y, w_y)$ [see Fig. 4(a)] to make the effective material parameters $C_{11}^{\text{eff}}, C_{22}^{\text{eff}}, \rho^{\text{eff}}$ of the SPS as close as possible to $C_{11}^S, C_{22}^S, \rho^S$ of Eq. (15) with $C_{11}^0, C_{66}^0, \rho^0$ being given. In addition, it should be noted that SPSs made of solids are inherently imperfect, which requires that the other two effective material parameters $C_{66}^{\text{eff}}, C_{12}^{\text{eff}}$ should also be as close as possible to 0 and $-\sqrt{C_{11}^S C_{22}^S}$, respectively. Thus, the optimization process can be divided into two steps [see Fig. 4(c)]. First, the initial geometric variables β_0, a_0, b_0 are optimized to satisfy the required anisotropy in Step 1. Then, on the basis of Step 1, the other four initial variables, l_{x0}, w_{x0}, l_{y0}, and w_{y0}, are optimized to form the final elasticity matrix. A dimensionless process is performed. All geometric parameters (except β)

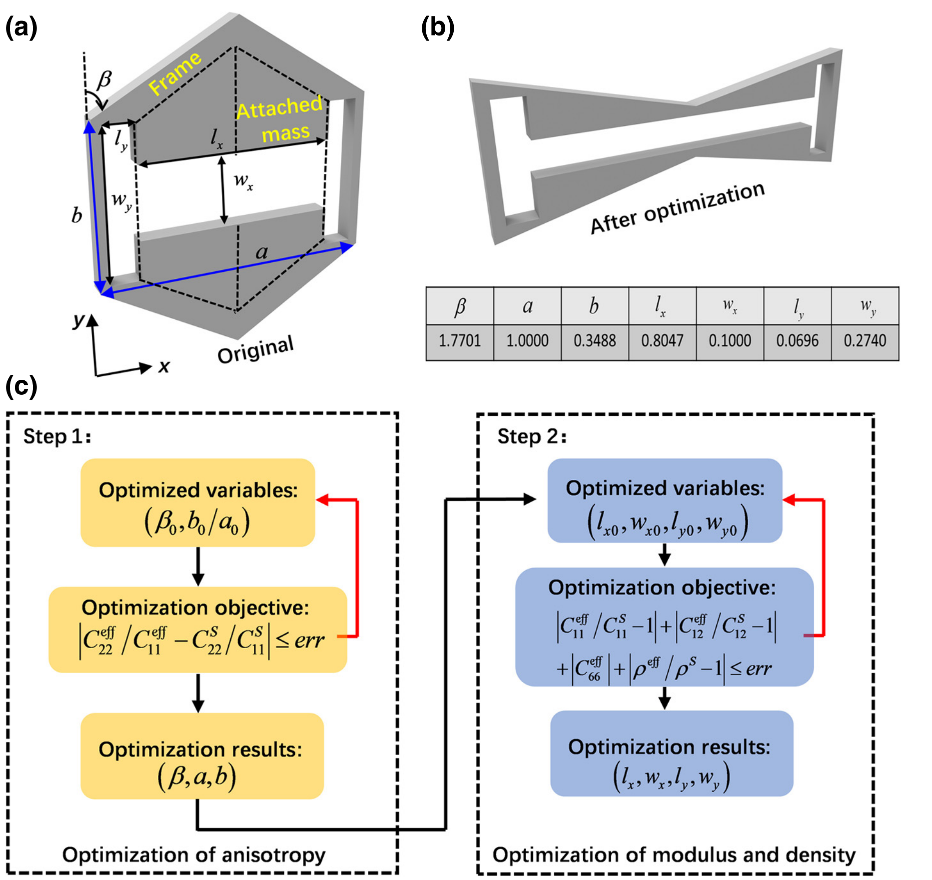

β	a	b	l_x	w_x	l_y	w_y
1.7701	1.0000	0.3488	0.8047	0.1000	0.0696	0.2740

FIG. 4. The microstructure design and optimization. (a) The proposed original microstructure. (b) The microstructure after optimization with the table showing the corresponding dimensionless geometric parameters. (c) Optimization steps.

TABLE I. The dimensionless effective material parameters, target theoretical parameters, and relative deviations.

Effective material properties of background medium	C_{11}^0	C_{22}^0	C_{12}^0	C_{66}^0	ρ^0
Values	0.2245	0.2245	0.0495	0.0290	0.4974
Target theoretical properties of SPS	C_{11}^S	C_{22}^S	C_{12}^S	C_{66}^S	ρ^S
Values	0.1952	0.0033	−0.0254	0	0.5720
Effective material properties of SPS	C_{11}^{eff}	C_{22}^{eff}	C_{12}^{eff}	C_{66}^{eff}	ρ^{eff}
Values	0.2039	0.0036	−0.0229	0.0007	0.5666
Relative deviations	4.3%	8.3%	11%	0.07%	0.95%

are divided by $\tilde{a} = 5$ mm (the lattice constant along the x direction), the densities ρ^{eff}, ρ^0 are divided by $\rho_{\text{Al}} = 2700$ kg/m^2 [the density of aluminum (Al)], and all effective modulus are divided by $C_{11} = 103$ GPa (the pressure wave modulus of Al). Finally, all of the dimensionless effective material parameters after optimization and their relative deviations from the target theoretical values [based on Eq. (15)] are given in Table I. It can be found that the average relative deviation of material parameters is less than 5%, which indicates the microstructure configuration after optimization is acceptable and can be used for experiments. The corresponding dimensionless geometric parameters after optimization are also listed in Fig. 4(b).

Here, it should be noted that it is very difficult to directly match the wave impedance between the SPS and Al since the SPS's unit cell [see Fig. 4(a)] is fabricated by perforating an Al plate. To solve this, the Al plate with circular holes ($\phi/d = 0.8$ with ϕ being the diameter of the circular hole and d being the size of the selected Al square) is used as a background medium and the corresponding effective elastic constants and density are regarded as $C_{11}^0, C_{66}^0, \rho^0$. Finally, a bow tielike microstructure with the desired anisotropy and wave impedance for the targeted polarized elastic wave propagations is shown in Fig. 4(b). Despite the irregular shape of the unit cell, multiple cells can still be arranged in a rectangular array without leaving any empty space between the neighboring cells. Total transmission and reflection can be achieved in the optimized SPS for L and T wave propagations along or off the principal axis, as shown in Figs. 3(a) and 3(b), respectively. It should also be noted that the size of the EMM unit cell can be further reduced as long as the fabrication precision permits.

IV. EXPERIMENTAL VALIDATION

Since the proposed SPSs do not rely on the resonant motion of the microstructure, elastic wave control with the SPSs are broadband in nature. To validate their polarization controllability, experimental characterizations are conducted.

A. Experiments setup

Figure 5 shows the experimental setup. Precision computer numerical control (CNC) machining is applied to fabricate the two types of anisotropic SPS arrays, which are called Type 1 and Type 2 corresponding to the fluidlike solid along the SPS's principal axis and the shear-wave

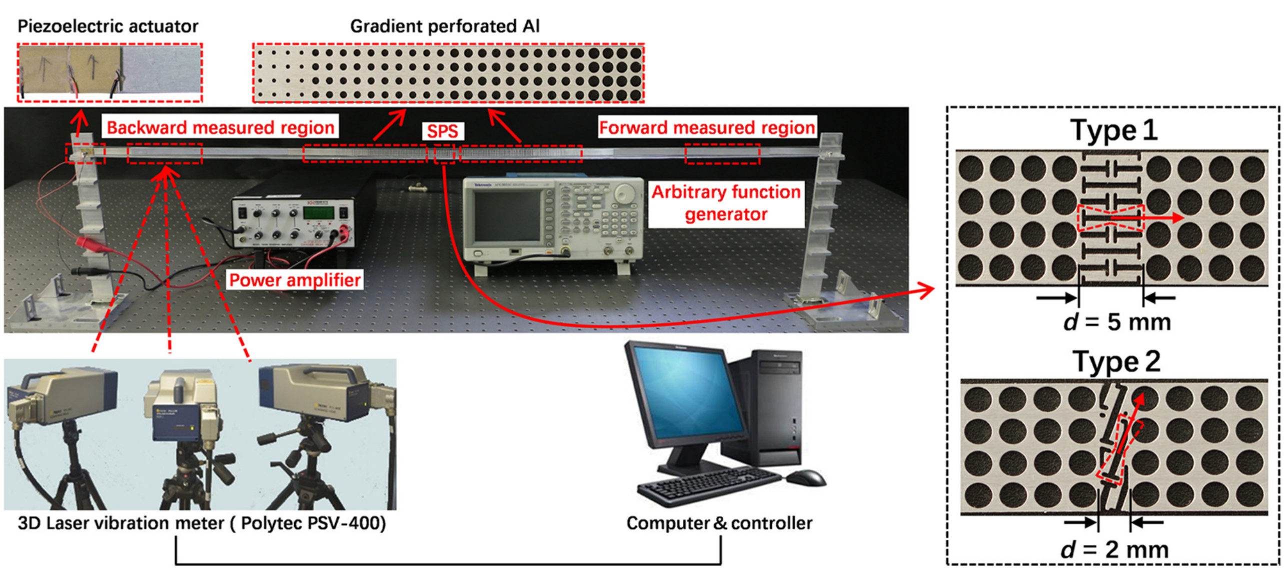

FIG. 5. The experimental setup and the enlarged views for the two types of SPS arrays.

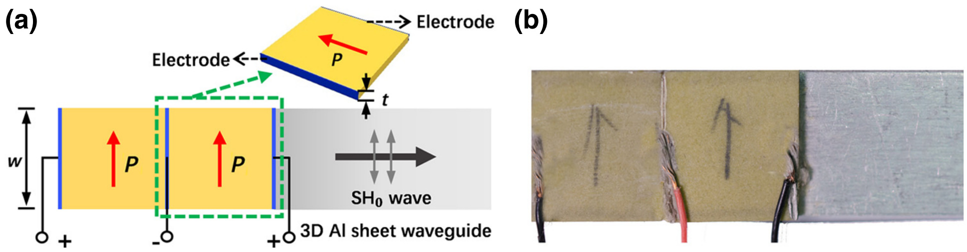

FIG. 6. The excitation of the SH_0 wave based on BSH PT. (a) Schematic of the BSH PT setup. (b) The photo of BSH PT in the experiments.

solid off the principal axis, respectively, as shown in the enlarged figure. The off-axis angle for Type 2 EMM is set as $\varphi \approx 70°$. The SPS arrays are located at the central portion of a 1.2 m × 0.01 m × 0.5 mm thin Al plate. It should be noted that the length of the array and the interfaces between the SPS patterns and the Al plate are determined by the following two rules: (1) minimum pattern sizes along the SPS's principal axes should be no smaller than the lattice constants and (2) manufacture feasibility for both SPS arrays should be guaranteed. Therefore, the pattern sizes for Type 1 and Type 2 SPSs are chosen as 5 and 2 mm, respectively. The unit cells along the principal axes of the two SPS types are marked by the red arrows. Due to the large density as well as the modulus difference between the solid Al plate portion and the perforated metamaterial pattern portion, it is very difficult to directly match their wave impedances by only adjusting the metamaterial's microstructures. To solve this, a series of holes with gradually changing radii is machined as a transition medium to bridge the Al and metamaterial portions and is symmetrically distributed on both sides of the metamaterial layer. The length of the entire plate is chosen to guarantee no interference from the plate's ends' wave reflections.

In the experiments, piezoelectric lead zirconate titanate (PZT) patches and a laser vibrometer are used to excite and receive elastic wave signals, respectively. For the wave excitation, special polarized wave generators are needed in the experiments for the required L and T wave incidences. PZT patches ($10 \times 10 \times 1$ mm^3) in d24 mode or in d31 mode are used at the left end of the plate for the pure T (SH_0 mode) or L (S_0 mode) wave generations, respectively [48,49]. In particular, the SH_0 waves are generated by the bidirectional SH_0 wave piezoelectric transducer (BSH PT) proposed by Miao *et al.* [48], since the BSH PT can generate a beam-focused pure SH_0 wave along the length direction of the Al plate while avoiding extra reflection of the SH_0 wave in the width direction. As shown in Fig. 6(a), the BSH PT consists of two identical square face-shear d24 mode PZT patches (side $w = 10$ mm, thickness $t = 1$ mm), which are bonded together via their lateral faces. The polarization directions [red arrow in Fig. 6(a)] of the two PZT patches are the same and they share the same electrode at the bonding interface. When an electric field is applied to the BSH PT, the induced opposite face-shear deformations of the two PZT patches generate the desired BSH wave. Since the BSH PT is placed at the end of the Al strip as shown in Fig. 6(b), a unidirectional SH_0 wave can be generated. Then a 3.5-cycle tone-burst signal with central frequency f_c is generated by a function generator (Tektronix AFG3021) and amplified by a wideband power amplifier (Krohn-Hite 7602M) for the voltage excitation. For the wave measurement, the in-plane displacements u_x and u_y in the marked backward and forward

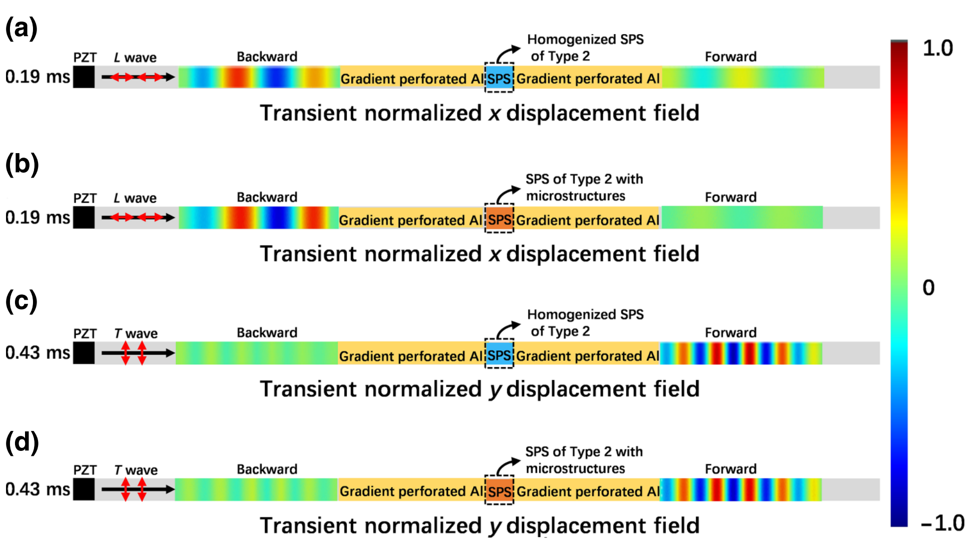

FIG. 7. The comparison of simulation results between a homogenized effective metamaterial and microstructures based on the Type 2 SPS. (a), (b) shows the transient displacement field with homogenized effective medium and microstructures, respectively, when the L wave is incident. (c), (d) shows the transient displacement field with homogenized effective medium and microstructures, respectively, when the T wave is incident.

regions are first measured by a 3D laser scanning vibrometer (Polytec PSV-400-3D) and then further processed in a computer for any necessary frequency-domain and wavenumber-domain signal processing [50,51].

B. Transient experimental results

Before the transient experimental measurement, finite element simulations are first conducted to verify whether the manufactured two SPS patterns can work as expected under the long wavelength condition. Full-wave transient simulations on the SPSs with detailed microstructures and the corresponding homogenized media are performed by using COMSOL Multiphysics software. In the simulation, the interaction between the PZT patches and the Al plate is considered within the Piezoelectric Devices Module. A 3.5-cycle tone-burst voltage signal (central frequency is 50 kHz), which is the same as the excitation signal in the experiment, is applied on the electrodes of the PZT patches. Compared with the Type 1 SPS array, the obliquely arranged unit cells of the Type 2 SPS lead to a much thinner array width and more complicated array boundary, which necessitates comparison with the homogenized medium. Figures 7(a) and 7(b) demonstrate

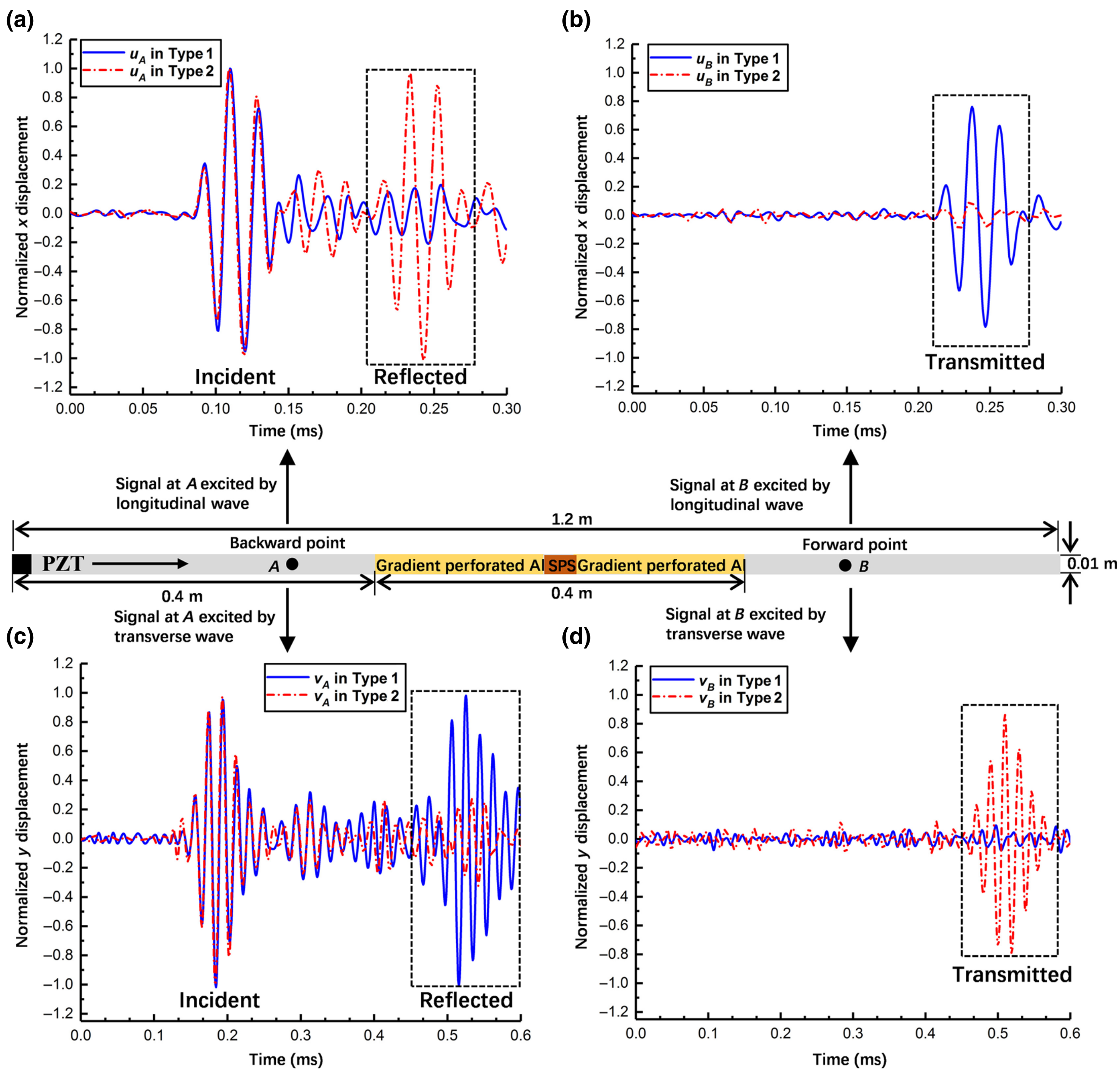

FIG. 8. The experimental results on the polarized elastic wave propagations in the designed SPSs. (a), (b) The time-domain x displacements measured at A (a) and B (b) points in Type 1 and Type 2 SPSs, respectively. (c), (d) The time-domain y displacements measured at A (c) and B (d) in Type 1 and Type2 SPSs, respectively.

the L-wave-incidence results for the two cases of manufactured microstructures and the homogenized medium, respectively. It can be found that in both cases, most parts of the incident L waves are reflected into the backward region and the transmitted L waves are extremely weak in the forward region. The corresponding transmissivities in Figs. 7(a) and 7(b) are 11.2% and 10.2%, respectively. Figures 7(c) and 7(d) demonstrate the T-wave-incidence results for the two cases. In both cases, almost all incident T waves are transmitted and the corresponding transmissivities are 93.0% and 90.2%, respectively. Thus, it is numerically verified that the manufactured Type 2 SPS pattern performs almost the same as its equivalent homogenized medium for the polarized waves' propagations. Since the Type 1 SPS array has more regular boundaries, the comparison results agree well as expected and are not shown here.

In the experiments, two measurement points A and B are selected in the backward and forward regions and the measured time-domain u_x and u_y results for the L and T waves incidences at $f_c = 50$ kHz are shown in Figs. 8(a), 8(b) and 8(c), 8(d), respectively. In these figures, the blue solid lines indicate the results for the Type 1 SPS while the red dashed lines indicate the results for the Type 2 SPS. For the L wave incidence, the Type 1 SPS performs like a transparent medium with almost no reflection at Point A and total transmission at Point B. On the contrary, the Type 2 SPS (obtained by rotating Type 1's principal axes) functions as a perfect reflector for the incident L wave, as shown in Figs. 8(a) and 8(b). When the incident wave is changed to a T wave, completely opposite results can be found in Figs. 8(c) and 8(d). Nearly total T wave reflection is found for the Type 1 SPS while very strong T wave transmission is observed for the Type 2 SPS.

It should be noted that the SH_0 wave generated by the face-shear deformations of the two PZT patches is equivalent to that caused by the induced shear stresses distributed along the PZT patch edges [52], so the induced unidirectional SH_0 wave is a superposition of wave signals from different edges and wave signals from the reflection in the 3D finite waveguide. As a result, compared with the signals of the S_0 wave in Figs. 8(a) and 8(b), the induced unidirectional SH_0 wave will have more cycles than drive signals as shown in Figs. 8(c) and 8(d).

Furthermore, snapshots of the normalized u_x and u_y fields measured in the forward region under L and T wave incidences are demonstrated in Figs. 9(a)–9(c) and 9(d)–9(f), respectively (six complete videos can be seen in the Supplemental Material [53]). The wave-field results measured at multiple time points are compared for the wave propagations in the following three media: the reference Al plate, the Type 1 SPS plate, and the Type 2 SPS plate. For the L wave incidence, it can be found in Figs. 9(a) and 9(b) that both the wave amplitudes and wave phases for the reference Al and Type 1 SPS plates are very close to each other, which indicates that neither wave attenuation nor wave dispersion is introduced by the SPS. However, almost no transmitted waves can be found at any time point for the Type 2 SPS plate in Fig. 9(c). For the T wave incidence, the measured wave-field results switch for the Type 1 and Type 2 SPS plates as expected. Compared with the reference wave field in Fig. 9(d), almost no transmitted wave fields can be found in Fig. 9(e) for the Type 1 SPS plate while both the wave amplitudes and wave phases

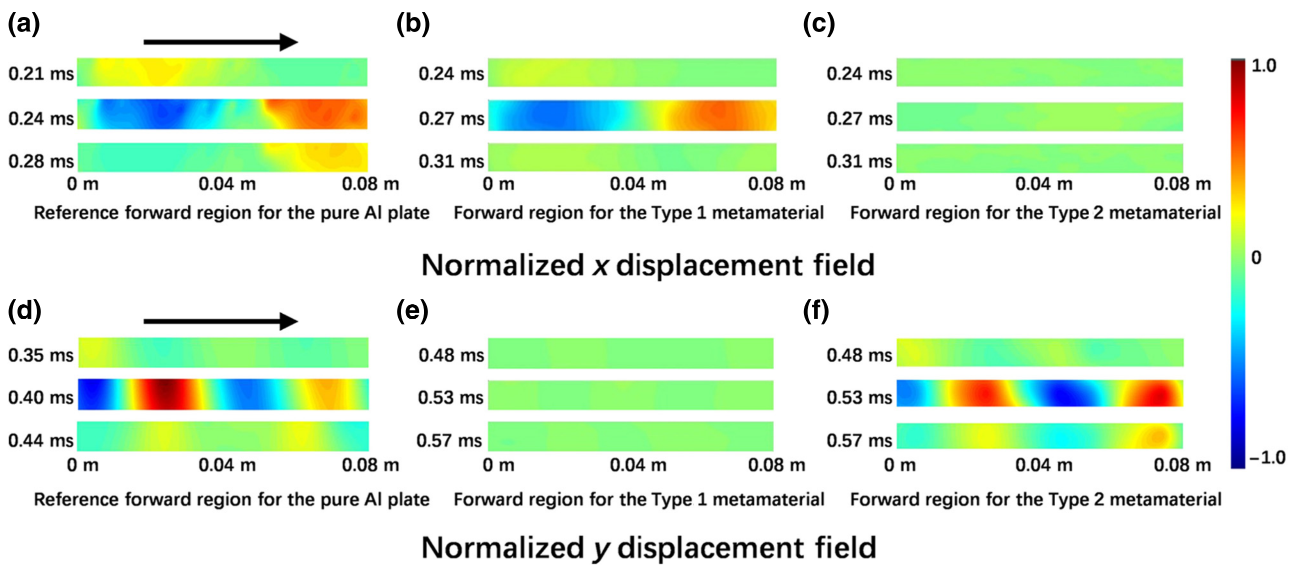

FIG. 9. Snapshots of the normalized u_x and u_y fields measured in the forward region. (a)−(c) Normalized x displacement fields measured in the forward regions in the reference plate (a), Type 1 SPS (b), and Type 2 SPS (c). (d)−(f) Normalized y displacement fields measured in the forward regions in the reference plate (d), Type 1 SPS (e), and Type 2 SPS (f).

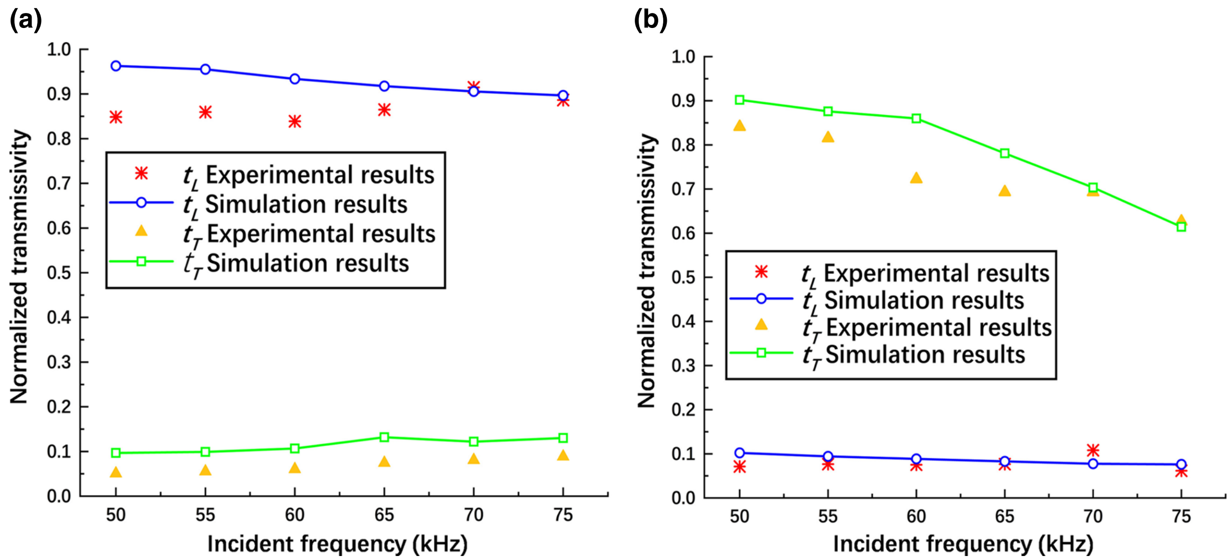

FIG. 10. The broadband polarized wave supportability of the SPSs. (a) Normalized L and T wave transmissivities in the Type 1 SPS plate at different frequencies. (b) Normalized L and T wave transmissivities in the Type 2 SPS plate at different frequencies.

are found almost unchanged in Fig. 9(f) for the Type 2 SPS plate, which indicates the total T wave transmission in the Type 2 SPS plate.

Since the two types of anisotropic SPS can be readily switched by just rotating the principal orientation, the above experiments successfully demonstrate that complete L or T wave control can be realized at a certain frequency with an engineered SPS, which has either "fluidlike solid" or "shear-wave solid" behaviors along the targeted propagation direction. Next, the broadband verification of this unique elastic wave polarization control capability will be tested.

C. Broadband verification

Transient wave experiments are conducted at different central frequencies sweeping from 50 to 75 kHz with a step of 5 kHz, as shown in Fig. 10. The transmission results obtained from numerical transient wave simulations are compared with the experimental results. In the figure, the normalized transmissivity is defined as $t_L = A_L^T/A_{0L}^T$ and $t_T = A_T^T/A_{0T}^T$, where, A_{0L}^T, A_{0T}^T and A_L^T, A_T^T denote the amplitudes of the transmitted L wave and T wave in the reference Al plate and the SPS plates, respectively. In general, the results demonstrate that the unique L or T wave control obtained by using the proposed anisotropic SPS

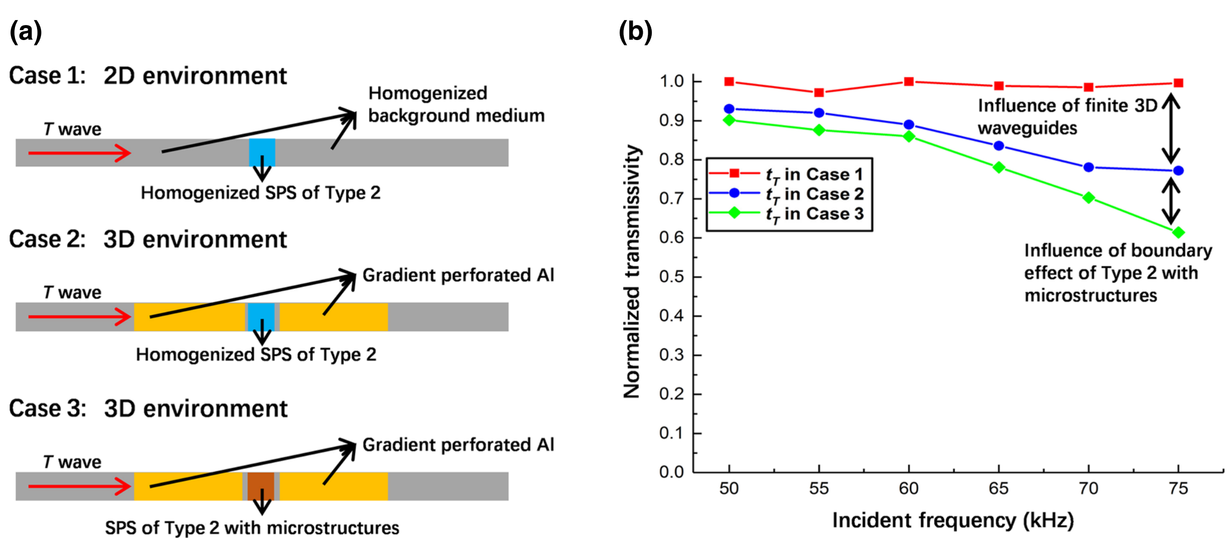

FIG. 11. The influence of frequency on the T wave transmissivity in the Type 2 SPS. (a) Schematic of different simulation environments. (b) The transmissivity with different frequencies in the three cases.

can be realized in a broad frequency range. The numerical and experimental results agree with each other quite well. In Fig. 10(a), the measured L wave transmissivity is above 84% while the measured T wave transmissivity is below 9% in the Type 1 SPS plate. Both measured results are lower than those obtained from the numerical simulations, which is due to the damping in experiments. In addition, the experimental measurement and signal sampling process also introduce a few unavoidable discrepancies. If the manufacture precision permits a minimum fillet radius and the lowest degree of inconsistency among all unit cells, theoretically, the transmissivities for the L wave and T wave can be very close to 100% and 0, respectively.

In Fig. 10(b), both experimental and numerical results of the T wave transmissivity in the Type 2 SPS plate decrease with the frequency. In order to explain the low T wave transmission in the high-frequency region, we qualitatively analyze the following three cases shown in Fig. 11(a). In Case 1, 2D simulations are conducted in homogenized media for both the Type 2 SPS and background medium with their upper and lower boundaries being set as periodic. In Case 2, 3D simulations are conducted in the homogenized plate of the Type 2 SPS and the gradient Al plate with all boundaries being set free, which actually forms a finite 3D waveguide. In Case 3, 3D simulations are conducted on the plate with both the Type 2 SPS and the gradient-perforated Al parts with exact microstructures and free boundaries. Figure 11(b) shows the transmissivities with different frequencies for the three cases. Compared with perfect transmission in Case 1, the T wave transmissivity decreases with frequency in Case 2, which indicates that the finite 3D waveguide especially affects the T wave transmissivity in the high-frequency region. While in Case 3, the interface effect of the SPS microstructures' pattern further decreases the T wave transmissivity at high frequencies. In summary, the influence of the finite 3D waveguide together with the interface effect of the SPS's microstructure lead to the decline of the T wave transmissivity in the high-frequency

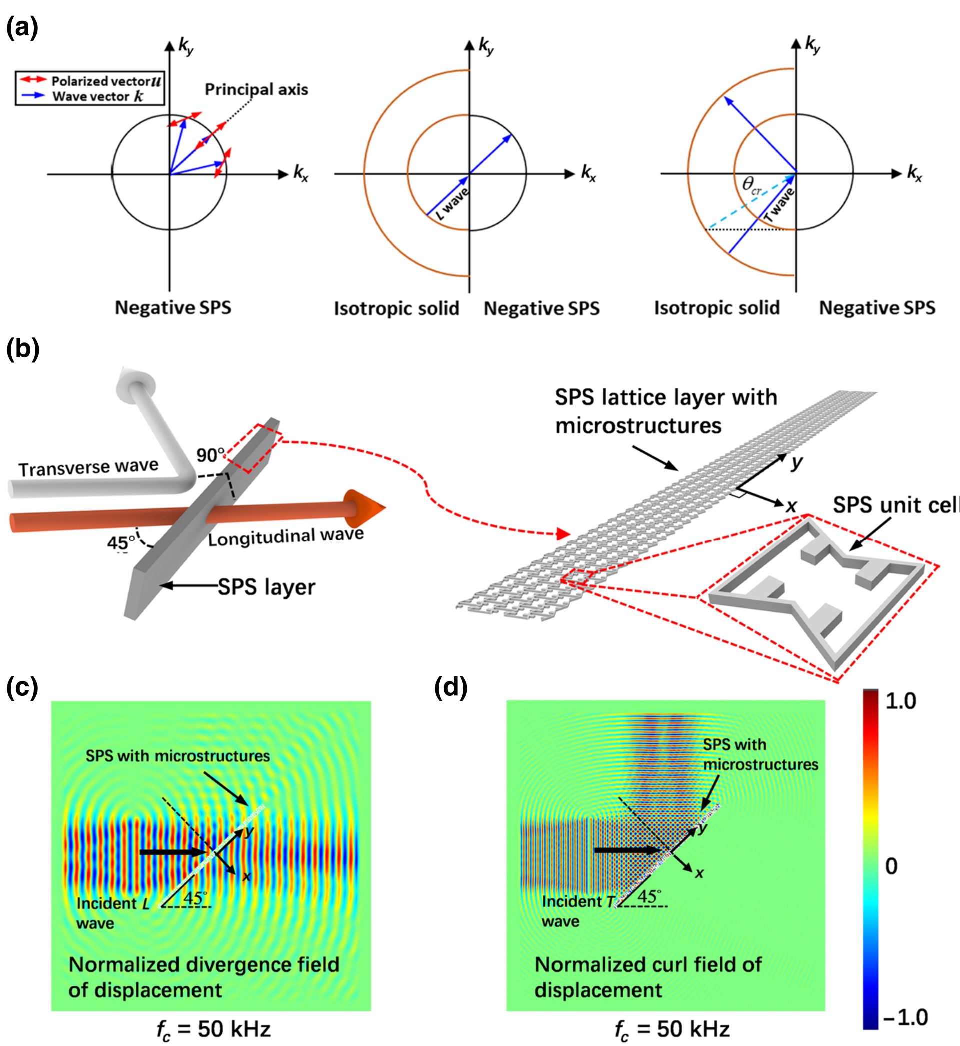

FIG. 12. 90° polarized wave splitter based on the proposed metamaterial. (a) EFC of the negative SPS with $C_{11}^S = C_{22}^S = C_{11}^0$. The analysis based on EFCs for the incident L wave case and incident T wave case, respectively. (b) Schematic of the 2D polarized wave splitter. The design with a metamaterial layer and microstructures. (c), (d) The simulation results show the normalized divergence and curl of displacement fields, respectively.

TABLE II. The dimensionless effective material parameters, target theoretical parameters, and relative deviations (Base material of SPS: Al; Background medium: Polypropylene. The dimensionless process and criterion are the same as before).

Material properties of background medium (Polypropylene)	C_{11}^0	C_{22}^0	C_{12}^0	C_{66}^0	ρ^0
Values	0.0204	0.0204	0.0142	0.0031	0.3296
Target theoretical properties of SPS	C_{11}^S	C_{22}^S	C_{12}^S	C_{66}^S	ρ^S
Values	0.0204	0.0204	−0.0204	0	0.3296
Effective material properties of SPS	C_{11}^{eff}	C_{22}^{eff}	C_{12}^{eff}	C_{66}^{eff}	ρ^{eff}
Values	0.0204	0.0205	−0.0204	0.0001	0.3296
Relative deviations	0%	0.49%	0%	0.01%	0%

region. A modified testing environment and advanced signal processing technology can be helpful. On the other side, the L wave transmissivity is kept below 10% for all measured frequency points, as shown in Fig. 10(b).

V. POTENTIAL APPLICATIONS FOR ELASTIC WAVE DEVICE

Based on the SPS's peculiar properties, we also explore its potential applications in alternative elastic wave devices, such as 90° polarized wave splitter and selective polarized wave focuser.

A. 90° broadband polarized wave splitter

In Fig. 12(a), the incident L wave comes from an isotropic solid (C_{11}^0, C_{66}^0, and ρ^0) through a thin negative SPS ($C_{11}^S = C_{22}^S = C_{11}^0$, $\rho^S = \rho^0$) layer. Based on the previous analysis, the EFC of the negative SPS is a circle, which coincides with the L wave EFC of the isotropic solid as shown in Fig. 12(a). Therefore, when an incident L wave comes from the isotropic solid into the SPS, the direction and amplitude of the refracted wave vector will not change due to the matched impedance. However, when an incident T wave comes from the isotropic solid into the SPS, total reflection of the T wave can be observed when the incident angle is greater than the critical angle ($\theta_{\text{cr}} = \sin^{-1}\sqrt{C_{66}^0/C_{11}^S}$). As a result, when L and T waves are both incident at 45° to the SPS layer, which is larger than $\theta_{\text{cr}} = 23°$, they are separated along two orthogonal directions. The detailed microstructures of the SPS and the corresponding simulation results are shown in Figs. 12(b)–12(d). The design parameters of the SPS are listed in Table II.

B. Selective broadband polarized wave focusing

Furthermore, selective polarized wave focusing can also be achieved with the negative SPS. By symmetrically placing the SPS layers on both sides of a line source, their tilt angles can be adjusted according to different working conditions. Since such a SPS layer has completely different transmission and reflection characteristics for a L wave and a T wave as demonstrated previously, the energy of the T wave can be focused at a specified position when a line source emits a T wave, as shown in Fig. 13(a). On the contrary, the energy of the L wave propagates away through the SPS layers when a line source emits a L wave, as shown in Fig. 13(b). This broadband selective polarized wave focusing can be very useful in the fields of energy harvesting, medical imaging, and so on.

VI. CONCLUSION

The proposed anisotropic SPS requires no resonant microstructures, and therefore, is naturally broadband. By just adjusting the principal orientation of the SPS, longitudinal-only or shear-only wave propagation can be achieved, which is experimentally validated. The size of the SPS unit cell is only 1/50 of the wavelength

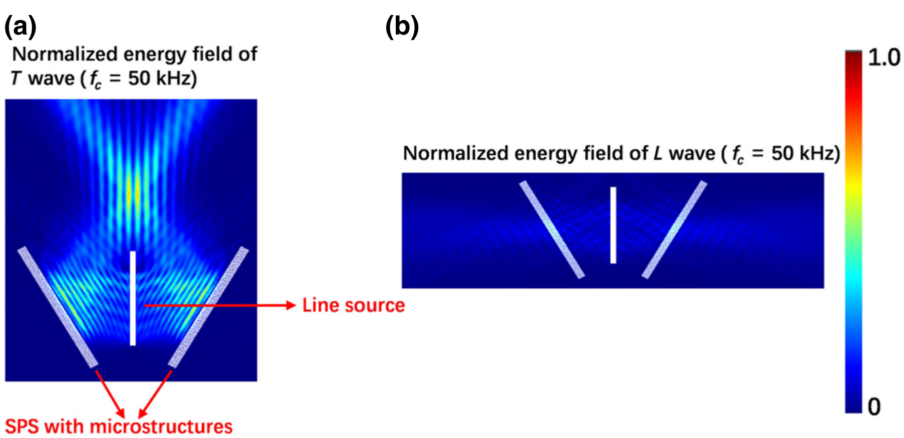

FIG. 13. Selective polarized wave focusing based on the proposed SPS. (a), (b) The simulation results show the normalized energy fields of the T wave and L wave, respectively (Base material of SPS: Al; Background medium: Polypropylene).

($f = 50$ kHz), which offers a deep subwavelength-scale elastic wave polarization controllability, which can be quite useful in various engineering fields. For example, a polarized wave splitter or focuser that can selectively separate or confine a L or T wave can lead to potential applications in nondestructive evaluation (NDE) or structural health monitoring (SHM). Finally, the nonresonant SPS can greatly expand the family of solid metamaterials and open up an alternative avenue for broadband elastic wave controlling and subwavelength elastic wave devices.

ACKNOWLEDGMENTS

This work was supported by the National Natural Science Foundation of China (NSFC) (Grants No. 11521062, No. 11632003, No. 11290153, and 111 project No. B16003). R.Z. also acknowledges support from NSFC Grants No. 11872112 and No. U1837602 and the Start-up fund from Beijing Institute of Technology. The authors thank Faxin Li from Peking University, Wei Zhang from Beijing University of Technology, and Xiaolin Wang from the Institute of Acoustic-CAS for their help in experimental device support.

M.Z. and X.L. contributed equally to this work.

APPENDIX A: INDEX CONTRACTION OF THE FOURTH-ORDER TENSOR C_{ijkl}

In the 2D case, Eq. (1) and the harmonic displacement can be expanded into the following formula

$$\begin{cases}\rho\ddot{u}_1 = C_{1111}u_{1,11} + C_{1121}u_{2,11} + C_{1112}u_{1,21} + C_{1122}u_{2,21} + C_{2111}u_{1,12} + C_{2121}u_{2,12} + C_{2112}u_{1,22} + C_{2122}u_{2,22},\\ \rho\ddot{u}_2 = C_{1211}u_{1,11} + C_{1221}u_{2,11} + C_{1212}u_{1,21} + C_{1222}u_{2,21} + C_{2211}u_{1,12} + C_{2221}u_{2,12} + C_{2212}u_{1,22} + C_{2222}u_{2,22},\end{cases} \tag{A1a}$$

$$\begin{cases}u_1 = U_1 e^{\mathrm{i}(-k_1x_1-k_2x_2+\omega t)},\\ u_2 = U_2 e^{\mathrm{i}(-k_1x_1-k_2x_2+\omega t)}.\end{cases} \tag{A1b}$$

And the index contraction of the fourth-order tensor C_{ijkl} is applied as follows:

$$\begin{cases}C_{1111} = C_{11},\\ C_{2222} = C_{22},\\ C_{1112} = C_{2111} = C_{1211} = C_{1121} = C_{16},\\ C_{2112} = C_{1212} = C_{2121} = C_{1221} = C_{66},\\ C_{1122} = C_{2211} = C_{12},\\ C_{2212} = C_{1222} = C_{2221} = C_{2122} = C_{26}.\end{cases} \tag{A2}$$

Thus, Eq. (2) in the main text can be obtained.

APPENDIX B: DERIVATION OF C_{11}^S AND C_{22}^S BASED ON THE IMPEDANCE MATCHING

For Case 1, the principal orientation of the SPS coincides with the reference coordinate system ($\varphi = 0$) and the elasticity matrix of SPS under the reference coordinate system is as follows:

$$C = \begin{bmatrix} C_{11}^S & -\sqrt{C_{11}^S C_{22}^S} & 0\\ -\sqrt{C_{11}^S C_{22}^S} & C_{22}^S & 0\\ 0 & 0 & 0\end{bmatrix}, \tag{B1}$$

Obviously, the T wave can be completely blocked because the impedance-supporting T wave in the SPS is zero. While in order to realize the complete transmission of the L wave, the impedance-supporting L wave between the SPS and background medium should match perfectly

$$\sqrt{C_{11}^S\rho^S} = \sqrt{C_{11}^0\rho^0}. \tag{B2}$$

For Case 2, there is an angle $\varphi = \tan^{-1}\sqrt[4]{C_{11}^S/C_{22}^S}$ between the principal orientation of the SPS and the reference coordinate system. Thus the elasticity matrix of the SPS under the reference coordinate system can be written in the following form based on the coordinate transformation of tensor($C'_{mnop} = \beta_{mi}\beta_{nj}\beta_{ok}\beta_{pl}C_{ijkl}$)

$$C' = \begin{bmatrix} 0 & 0 & 0\\ 0 & \left(\sqrt{C_{11}^S} - \sqrt{C_{22}^S}\right)^2 & \left(\sqrt{C_{11}^S} - \sqrt{C_{22}^S}\right)\sqrt[4]{C_{11}^S C_{22}^S}\\ 0 & \left(\sqrt{C_{11}^S} - \sqrt{C_{22}^S}\right)\sqrt[4]{C_{11}^S C_{22}^S} & \sqrt{C_{11}^S C_{22}^S}\end{bmatrix}, \tag{B3}$$

where $\beta = \begin{bmatrix} \cos\varphi & -\sin\varphi \\ \sin\varphi & \cos\varphi \end{bmatrix}$ and $\varphi = \tan^{-1}\sqrt[4]{C_{11}^S/C_{22}^S}$. Similarly, in this case, the L wave can be complete blocked because the impedance-supporting L wave in the SPS is zero. We can make the impedance-supporting T wave between the SPS and background medium match perfectly to achieve total transmission of the T wave

$$\sqrt{\sqrt{C_{11}^S C_{22}^S}\rho^S} = \sqrt{C_{66}^0 \rho^0}. \tag{B4}$$

By combining Eqs. (B2) and (B4), we can easily get

$$\begin{cases} C_{11}^S = (\rho^0/\rho^S) C_{11}^0, \\ C_{22}^S = (\rho^0/\rho^S)(C_{66}^0)^2/C_{11}^0. \end{cases}$$

[1] J. L. Rose, *Ultrasonic Guided Waves in Solid Media* (Cambridge University Press, Cambridge, 2014).

[2] D. N. Alleyne and P. Cawley, The interaction of Lamb waves with defects, IEEE Trans. Ultrason. Ferroelectr. Freq. Control **39**, 381 (1992).

[3] G. Ma, C. Fu, G. Wang, P. Del Hougne, J. Christensen, Y. Lai, and P. Sheng, Polarization bandgaps and fluid-like elasticity in fully solid elastic metamaterials, Nat. Commun. **7**, 13536 (2016).

[4] S. H. Mousavi, A. B. Khanikaev, and Z. Wang, Topologically protected elastic waves in phononic metamaterials, Nat. Commun. **6**, 8682 (2015).

[5] B. F. Kennedy, P. Wijesinghe, and D. D. Sampson, The emergence of optical elastography in biomedicine, Nat. Photonics **11**, 215 (2017).

[6] Z. Liu, X. Zhang, Y. Mao, Y. Y. Zhu, Z. Yang, C. T. Chan, and P. Sheng, Locally resonant sonic materials, Science **289**, 1734 (2000).

[7] S. Yao, X. Zhou, and G. Hu, Experimental study on negative effective mass in a 1D mass-spring system, New J. Phys. **10**, 043020 (2008).

[8] N. Fang, D. Xi, J. Xu, M. Ambati, W. Srituravanich, C. Sun, and X. Zhang, Ultrasonic metamaterials with negative modulus, Nat. Mater. **5**, 452 (2006).

[9] C. M. Soukoulis and M. Wegener, Past achievements and future challenges in the development of three-dimensional photonic metamaterials, Nat. Photonics **5**, 523 (2011).

[10] R. A. Shelby, D. R. Smith, and S. Schultz, Experimental verification of a negative index of refraction, Science **292**, 77 (2001).

[11] D. Schurig, J. J. Mock, B. J. Justice, S. A. Cummer, J. B. Pendry, A. F. Starr, and D. R. Smith, Metamaterial electromagnetic cloak at microwave frequencies, Science **314**, 977 (2006).

[12] H. Chen, C. T. Chan, and P. Sheng, Transformation optics and metamaterials, Nat. Mater. **9**, 387 (2010).

[13] S. A. Cummer, J. Christensen, and A. Alù, Controlling sound with acoustic metamaterials, Nat. Rev. Mater. **1**, 16001 (2016).

[14] G. Ma and P. Sheng, Acoustic metamaterials: From local resonances to broad horizons, Sci. Adv. **2**, e1501595 (2016).

[15] T. Brunet, A. Merlin, B. Mascaro, K. Zimny, J. Leng, O. Poncelet, C. Aristégui, and O. Mondain-Monval, Soft 3D acoustic metamaterial with negative index, Nat. Mater. **14**, 384 (2015).

[16] Z. Chang, H. Y. Guo, B. Li, and X. Q. Feng, Disentangling longitudinal and shear elastic waves by neo-Hookean soft devices, Appl. Phys. Lett. **106**, 161903 (2015).

[17] Y. Wu, Y. Lai, and Z. Q. Zhang, Elastic Metamaterials with Simultaneously Negative Effective Shear Modulus and Mass Density, Phys. Rev. Lett. **107**, 105506 (2011).

[18] X. Su, Z. Lu, and A. N. Norris, Elastic metasurfaces for splitting SV-and P-waves in elastic solids, J. Appl. Phys. **123**, 91701 (2018).

[19] H. J. Lee, J. R. Lee, S. H. Moon, T. J. Je, E. C. Jeon, K. Kim, and Y. Y. Kim, Off-centered double-slit metamaterial for elastic wave polarization anomaly, Sci. Rep. **7**, 15378 (2017).

[20] B. Ahn, H. J. Lee, and Y. Y. Kim, Topology optimization of anisotropic metamaterials tracing the target EFC and field polarization, Comput. Methods Appl. Mech. Eng. **333**, 176 (2018).

[21] X. Zhou and G. Hu, Analytic model of elastic metamaterials with local resonances, Phys. Rev. B **79**, 195109 (2009).

[22] K. Kim, C. Il Park, H. Lee, and Y. Y. Kim, Near-zero effective impedance with finite phase velocity for sensing and actuation enhancement by resonator pairing, Nat. Commun. **9**, 5255 (2018).

[23] X. N. Liu, G. K. Hu, G. L. Huang, and C. T. Sun, An elastic metamaterial with simultaneously negative mass density and bulk modulus, Appl. Phys. Lett. **98**, 251907 (2011).

[24] X. N. Liu, G. L. Huang, and G. K. Hu, Chiral effect in plane isotropic micropolar elasticity and its application to chiral lattices, J. Mech. Phys. Solids **60**, 1907 (2012).

[25] R. Zhu, X. N. Liu, and G. L. Huang, Study of anomalous wave propagation and refletion in semi-infinite elastic metamaterials, Wave Motion **55**, 73 (2015).

[26] Y. Lai, Y. Wu, P. Sheng, and Z. Q. Zhang, Hybrid elastic solids, Nat. Mater. **10**, 620 (2011).

[27] R. Zhu, X. N. Liu, G. K. Hu, C. T. Sun, and G. L. Huang, Negative refraction of elastic waves at the deep-subwavelength scale in a single-phase metamaterial, Nat. Commun. **5**, 5510 (2014).

[28] R. Zhu, H. Yasuda, G. L. Huang, and J. K. Yang, Kirigami-based elastic metamaterials with anisotropic mass density for subwavelength flexural wave control, Sci. Rep. **8**, 483 (2018).

[29] A. Colombi, P. Roux, S. Guenneau, and M. Rupin, Directional cloaking of flexural waves in a plate with a locally resonant metamaterial, J. Acoust. Soc. Am. **137**, 1783 (2015).

[30] A. Foehr, O. R. Bilal, S. D. Huber, and C. Daraio, Spiral-Based Phononic Plates: From Wave Beaming to Topological Insulators, Phys. Rev. Lett. **120**, 205501 (2018).

[31] R. Chaunsali, C. Chen, and J. Yang, Subwavelength and directional control of flexural waves in zone-folding induced topological plates, Phys. Rev. B **97**, 54307 (2018).

[32] Y. Chen, X. Liu, and G. Hu, Topological phase transition in mechanical honeycomb lattice, J. Mech. Phys. Solids **122,** 54 (2019).
[33] M. Badreddine Assouar and M. Oudich, Enlargement of a locally resonant sonic band gap by using double-sides stubbed phononic plates, Appl. Phys. Lett. **100**, 123506 (2012).
[34] S. Krödel, N. Thomé, and C. Daraio, Wide band-gap seismic metastructures, Extrem. Mech. Lett. **4**, 111 (2015).
[35] J. M. Kweun, H. J. Lee, J. H. Oh, H. M. Seung, and Y. Y. Kim, Transmodal Fabry-Pérot Resonance: Theory and Realization with Elastic Metamaterials, Phys. Rev. Lett. **118**, 205901 (2017).
[36] X. Yang, J. M. Kweun, and Y. Y. Kim, Theory for perfect transmodal Fabry-Perot interferometer, Sci. Rep. **8**, 69 (2018).
[37] X. Yang and Y. Y. Kim, Topology optimization for the design of perfect mode-converting anisotropic elastic metamaterials, Compos. Struct. **201**, 161 (2018).
[38] G. W. Milton and A. V. Cherkaev, Which Elasticity Tensors are Realizable?, J. Eng. Mater. Technol. **117**, 483 (1995).
[39] G. W. Milton, Complete characterization of the macroscopic deformations of periodic unimode metamaterials of rigid bars and pivots, J. Mech. Phys. Solids **61**, 1543 (2013).
[40] G. W. Milton, Adaptable nonlinear bimode metamaterials using rigid bars, pivots, and actuators, J. Mech. Phys. Solids **61**, 1561 (2013).
[41] X. Zheng, Howon Lee, Todd H. Weisgraber, Maxim Shusteff, Joshua DeOtte, Eric B. Duoss, Joshua D. Kuntz, Monika M. Biener, Qi Ge, Julie A. Jackson, Sergei O. Kucheyev, Nicholas X. Fang, and Christopher M. Spadaccini, Ultralight, ultrastiff mechanical metamaterials, Science **344**, 1373 (2014).
[42] M. Kadic, T. Bückmann, N. Stenger, M. Thiel, and M. Wegener, On the practicability of pentamode mechanical metamaterials, Appl. Phys. Lett. **100**, 191901 (2012).
[43] T. Bückmann, M. Thiel, M. Kadic, R. Schittny, and M. Wegener, An elasto-mechanical unfeelability cloak made of pentamode metamaterials, Nat. Commun. **5**, 4130 (2014).
[44] C. N. Layman, C. J. Naify, T. P. Martin, D. C. Calvo, and G. J. Orris, Highly Anisotropic Elements for Acoustic Pentamode Applications, Phys. Rev. Lett. **111**, 24302 (2013).
[45] C. W. Cushing, M. R. Haberman, P. S. Wilson, X. Su, and A. N. Norris, Experimental validation of the underwater sound focusing properties of a pentamode gradient index metamaterial lens, J. Acoust. Soc. Am. **140**, 3048 (2016).
[46] Y. Chen, M. Zheng, X. Liu, Y. Bi, Z. Sun, P. Xiang, J. Yang, and G. Hu, Broadband solid cloak for underwater acoustics, Phys. Rev. B **95**, 180104 (2017).
[47] Y. Chen, X. Liu, and G. Hu, Latticed pentamode acoustic cloak, Sci. Rep. **5**, 15745 (2015).
[48] H. Miao, H. Qiang, F. Li, and G. Kang, A variable-frequency bidirectional shear horizontal (SH) wave transducer based on dual face-shear (d24) piezoelectric wafers, Ultrasonics **89**, 13 (2018).
[49] R. Zhu, G. L. Huang, H. H. Huang, and C. T. Sun, Experimental and numerical study of guided wave propagation in a thin metamaterial plate, Phys. Lett. A **375**, 2863 (2011).
[50] M. Ruzzene, Frequency–wavenumber domain filtering for improved damage visualization, Smart Mater. Struct. **16**, 2116 (2007).
[51] M. Ruzzene, B. Xu, J. L. Sang, T. E. Michaels, and J. E. Michaels, Damage visualization via beamforming of frequency-wavenumber filtered wavefield data, Proc. SPIE - Int. Soc. Opt. Eng. **7650**, 76500L (2010).
[52] H. Miao, L. Xu, H. Zhang, and G. Kang, Controllable SH wave radiation patterns generated by finite-size face-shear piezoelectric transducers for structural health monitoring, arXiv Prepr. arXiv1811.06812 (2018).
[53] See Supplemental Material at http://link.aps.org/supplemental/10.1103/PhysRevApplied.12.014027 for six videos on the measured x-/y-displacement fields in the forward regions for reference Al plate, Type 1 metamaterial and Type 2 metamaterial.